Article

Microstructure and Wear Resistance of Hot-Work Tool Steels after Electron Beam Surface Alloying with B_4C and Al

Undrakh Mishigdorzhiyn [1], Aleksandr Semenov [1], Nikolay Ulakhanov [1,2,*], Aleksandr Milonov [1], Dorzho Dasheev [1] and Pavel Gulyashinov [1,3]

1 Institute of Physical Materials Science of the Siberian Branch of the Russian Academy of Sciences, 670047 Ulan-Ude, Russia; mishigdorzh@gmail.com (U.M.); semenov@ipms.bscnet.ru (A.S.); terwer81@mail.ru (A.M.); fokter@mail.ru (D.D.); gulpasha@mail.ru (P.G.)
2 Department of Mechanical Engineering, East Siberia State University of Technology and Management, 670013 Ulan-Ude, Russia
3 Baikal Institute of Nature Management of the Siberian Branch of the Russian Academy of Sciences, 6 Sakhyanovoy Street, 670047 Ulan-Ude, Russia
* Correspondence: nulahanov@mail.ru

Abstract: (1) Background: Operational properties and durability of dies in different metal-forming processes significantly depend on their surface quality. Major die failures are related to surface damage due to heat checking cracks, wear, etc. Thereby, strengthening of the working surfaces of dies for hot bending, stamping, forging, and die casting processes is an urgent engineering challenge. Surface alloying with high-energy beams improves the properties of steel products. In these processes, the alloying powders and the treated surfaces can be remelted by electron beam within a short time while the bulk structure of the component remains unchanged, resulting in minimal distortion. The paper presents the results of the electron beam surface alloying (EBSA) of H21 and L6 tool steels with the treatment pastes containing boron carbide and aluminum powders. (2) Methods: Two types of pastes were used for surface alloying: a single-component (B_4C) paste and a two-component (B_4C+Al) one. The microstructure, microhardness, wear resistance, and elemental and phase composition of the layers obtained on steels were investigated. (3) Results: Four layers up to 0.4 mm thick were distinguished on the surface of the steels after the EBSA. Metallographic analysis showed coarse dendrite formation in the layers embedded in matrices of a eutectic or a solid solution. Microhardness of the steels after the two-component EBSA was higher than after B_4C EBSA, which was related to a higher concentration of hard phases, such as iron borides and carbides. In addition, aluminum boride was revealed by the XRD analysis on L6 steel after B_4C+Al EBSA. (4) Conclusions: Wear test indicated that the most resistant samples were H21 steel after single B_4C EBSA and L6 steel after B_4C+Al EBSA. Both samples contained carbon particles in the layer contributing to the high wear resistance as a lubricant. The conducted research is beneficial for mechanical engineering, automotive engineering, medical technology, aerospace engineering, and related industries, where coatings with high microhardness, wear resistance, and surface quality are demanded.

Keywords: electron beam; surface alloying; boron carbide; aluminum; XRD; spectral analysis; borides; microhardness

1. Introduction

One of the methods of surface engineering is electron beam surface alloying (EBSA), which implies heating by an electron beam (EB) above the melting point of the treated surface and alloying compound. The obtained mechanical properties, including wear resistance, depend on the composition of the alloying mixture and the parameters of the electron beam [1].

The EB has a well-known wide range of effects, including a rise in temperature, relaxation, and diffusion processes in the metal. During the EBSA, various physicochemical

processes occur on the metal surface due to simultaneous temperature increase, charged particles flow, and alloying elements on it. Along with the temperature growth, changes occur in the crystal lattice, which determine fundamentally various processes, different from those of the conventional thermal-chemical treatment (TCT), transforming the method of layer formation from diffusion to diffusion-crystallization [2].

Another advantage of the EBSA is a vacuum media preventing different undesirable processes on the surface, such as oxidation. All of the above-mentioned features result in layers with a particular structure unobtainable by the common TCT in a furnace. Krukovitch et al. reported on the special composite structure of the boride layer after electron beam remelting [3]. The brittleness of such a layer was reduced by 1.5 times compared to the pack boriding. It is known that the pack boriding with furnace heating leads to layers with acicular or tooth-like structures. This type of layer works perfectly for abrasive wear in acid and humid media. However, the increased fragility of these layers restricts further boriding application in other processes such as forging, stamping, die-casting, etc., where high impact and thermal shock loading are applied to the surface of the dies [4]. Ostapenko et al. reported about residual stresses relaxation on the surface of TiNi substrate by a low-energy high-current electron beam [5]. H21 and L6 die steels are among the most widely used materials in the aforementioned manufacturing processes. Plastic deformation, wear, and fatigue are the most common failures of the dies in hot forging [6]. The latter two failures occur on the surface. It is known that 80% of the dies break due to heat-checking cracks initiating from the surface of hot working tools [7]. Thereby, strengthening the working surfaces of dies for hot bending/stamping processes or injection molding is an urgent engineering challenge. Boron is known for its capacity to form hard compounds in steels and alloys during different surface engineering techniques: TCT, laser, EB, plasma, electrochemical, etc. [8–14]. It is possible to combine two or three techniques to modify the previously obtained coating/diffusion layer and achieve properties unattainable by a single treatment [15–18].

One more option is to add other chemical elements to the boron-containing media. In this case, multicomponent boriding is capable of setting off pure boriding drawbacks, such as high brittleness [19,20].

Thus, the purpose of this research is to improve the mechanical properties of H21 and L6 die steels by means of the EBSA with single B_4C and two-component B_4C-Al pastes in a vacuum. This work sheds light on enhancing tribological properties of the obtained layers, particularly on wear resistance and wear mechanism. The novelty of the paper is a new approach for producing boron- and aluminum-containing layers on the surface of tool steels under high-energy beams in a vacuum.

2. Materials and Methods

Specific requirements for the materials such as high strength and thermal stability are used to manufacture die tooling. The first requirement allows retaining a die shape at high specific pressures during deformation. The second one preserves high hardness and strength during long-term temperature exposure. In addition, die steels must have high hardenability to provide the necessary mechanical properties throughout the entire section. For instance, sufficient toughness is necessary to prevent breakage under impact loading while deforming workpieces.

High heat and thermal fatigue resistance are necessary for hot forging dies to withstand a network of cracks during repeated heating and cooling processes.

High-quality hot work tool steel such as H21 and L6 steels with chromium, nickel, and other alloying elements are being used to meet all those requirements. Full chemical composition is given in Tables 1 and 2 [21,22].

The wear of the working surfaces of forging or stamping dies in most cases is uneven. Areas with a higher speed of metal flow during the deformation process are subjected to intense degradation. For instance, the most vulnerable surface of a U-bending die is its shoulder on the edge of the tool as shown in Figure 1a,b [23]. In this regard, increasing the

durability of a die will be enough to modify those surfaces. The EBSA in vacuum looks to be reasonable to provide local treatment, according to the scheme shown in Figure 1c.

Table 1. The chemical composition of H21 steel, wt %.

C	Si	Mn	P	S	Cr	W	V	Fe
0.26–0.36	0.15–0.5	0.15–0.4	up to 0.03	up to 0.03	3.0–3.75	8.5–10	0.3–0.6	84.33–87.58

Table 2. The chemical composition of L6 steel, wt %.

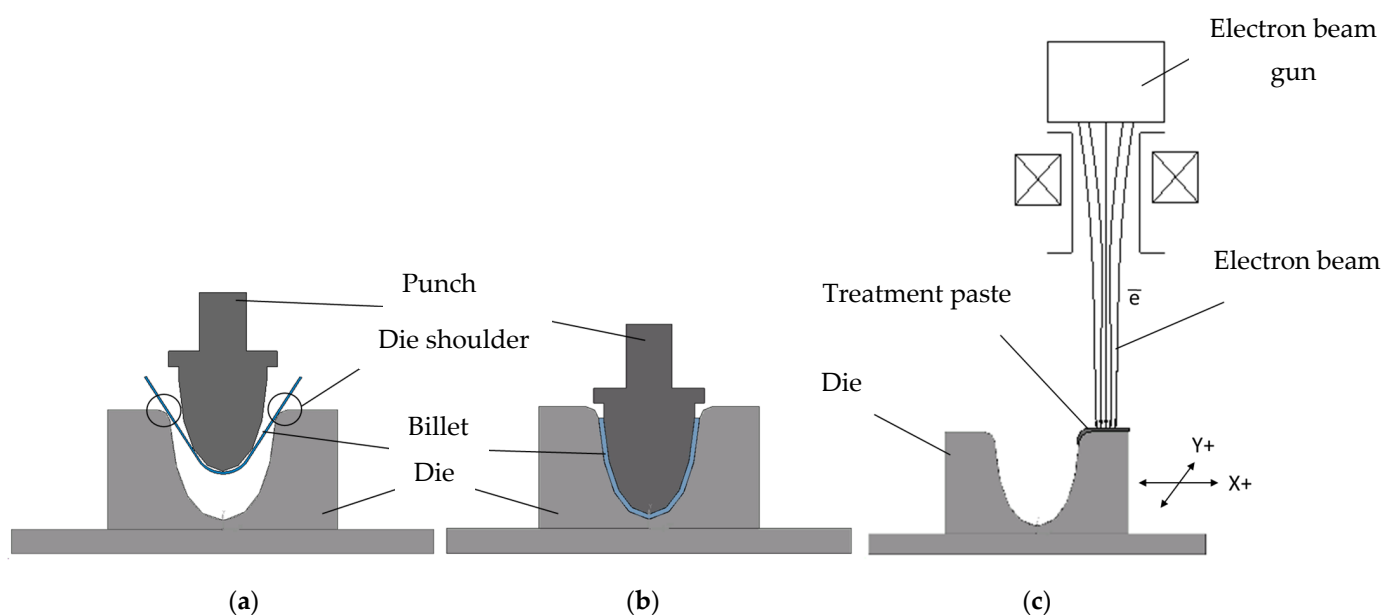| C	Si	Mn	Ni	S	P	Cr	Mo	Fe
0.65–0.75	0.10–0.5	0.25–0.8	1.25–2	up to 0.03	up to 0.03	0.6–1.2	up to 0.5	94.19–97.15

Figure 1. U-type profile formation during bending procedure: (**a**) initial positioning; (**b**) final shape; (**c**) EB processing of U-bending die with a treatment paste.

The EB processing was carried out using a vacuum installation with EPA-60-04.2 axial electron gun, a BUEL control unit, a high-voltage rectifier, and a vacuum supply system [24]. In the present research, rectangular samples of H21 and L6 steels with nominal dimensions of $20 \times 12 \times 10 \pm 1/2$ mm (l × w × h) were chosen as test material. Four major faces on each of the samples were ground to 1000 grit. Finally, the samples were rinsed in ethyl alcohol, dried, and coated with a treatment paste containing powders of pure boron carbide or boron carbide with aluminum in the following proportions: 0.8 B_4C + 0.2 Al. Previous investigations showed that the latter paste composition led to the boroaluminized layer with heterogeneous structure and high wear resistance on H21 steel. It is necessary to point out that the diffusion layer was obtained after long exposure for 2 h at 1050 °C in a muffle furnace [19].

The powders with organic glue were mixed to obtain the paste. The obtained paste of 0.5–1.0 mm thick was distributed over the treated surface and dried before EB processing. Heating was carried out by continuous EB for 36–115 s at the specific beam density of 5.7×10^2 W/mm². Due to the low Al melting point, the two-component paste demanded a shorter EB treatment time to melt on the surface. The EB processing modes were as follows: accelerating voltage of 24 kV, EB current of 20 mA, EB diameter of 1 mm, and sweep frequency of 50 Hz. The residual pressure in the vacuum chamber did not exceed 2×10^{-3} Pa. Tables 3 and 4 list the weights of the uncoated and coated with paste samples,

before and after the EBSA as well as the processing time for each sample. The samples' weight increased after the EBSA, which evidenced that the surface alloying of steels with saturating components took place [25].

Table 3. Samples' weight change before and after the EBSA on H21 steel.

Sample No. and Paste Type	Sample Weight, g	Weight with the Paste before EB Treatment, g (Weight Gain)	Weight after the EBSA, g (Weight Gain)	Treatment Time, s
1. B_4C	8.9615	8.9993 (+0.0378)	8.9804 (+0.0189)	115
2. B_4C+Al	8.3262	8.3743 (+0.0481)	8.3295 (+0.0033)	36

Table 4. Samples' weight change before and after the EBSA on L6 steel.

Sample No. and Paste Type	Sample Weight, g	Weight with the Paste before EB Treatment, g (Weight Gain)	Weight after the EBSA, g (Weight Gain)	Treatment Time, s
3. B_4C	9.3693	9.4062 (+0.0369)	9.3933 (+0.024)	115
4. B_4C+Al	9.0249	9.0761 (+0.0512)	9.0443 (+0.0194)	57

The treated samples were cross-sectioned and subjected to a conventional metallographic preparation procedure. The microstructure of the samples was studied with a METAM RV-22 metallographic microscope and a JEOL JSM-6510LV scanning electron microscope (SEM) with an acceleration voltage of 20 keV at the Science Center "Progress" of East Siberia State University of Technology and Management, Ulan-Ude, Russia (ESSUTM). Energy-dispersive X-ray spectroscopy (EDS) analysis was carried out by an Oxford Instruments INCA Energy 350 microanalysis system mounted on the JEOL JSM-6510LV SEM. The phase composition was determined by an X-ray diffractometer (XRD) Bruker Phaser 2D in copper radiation with a shooting interval of 10–85°. Microhardness was measured by a PMT-3M microhardness tester at a load of 0.5 N.

Wear resistance was examined by an SMTs-2 friction machine after loading the samples for a given time and measuring mass loss rate of the samples [26]. The test was conducted according to the block-on-ring scheme with dry sliding friction to simulate two-body sliding abrasive wear as shown in Figure 2. The sample was attached fixedly in the holder, and the counter body rotated at a certain speed. The counter body was a hardened disk of the high-speed steel with a hardness of 63 ± 2 HRC, the sliding speed was 0.8 m/s (n = 300 min^{-1}), and the contact pressure was 6.86 N/mm^2 [19]. The test samples of the tool steels were subjected to the EBSA in alignment with the aforementioned EB processing modes. In addition, the bare steels were also tested for comparison after the heat treatment. An analytical scale AXIS AGN-200 with an accuracy of $\pm10^{-4}$ g was used to measure mass loss every one, five, or ten minutes depending on the samples' hardness. The worn surfaces were examined by the SEM and EDS analysis after the test was over.
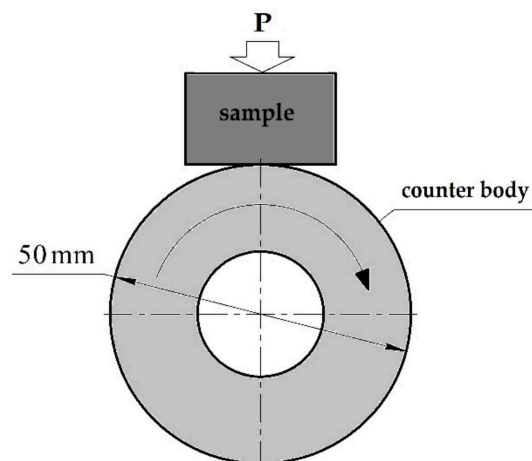
Figure 2. The block-on-ring scheme of the wear resistance test [19].

3. Results

Metallographic analysis showed that the EBSA resulted in homogeneous layer formation without zoning (layering) as shown in Figure 3. The alloyed layer's thickness on both steels was roughly the same. The layer thickness on H21 steel was 370–380 μm and 350–370 μm after single-B$_4$C EBSA and two-component B$_4$C+Al EBSA correspondingly, while for L6 steel it was 350–360 μm and 340–350 μm after single B$_4$C EBSA and two-component B$_4$C+Al EBSA, respectively. High roughness was observed on the surface of the layers except for H21 steel after single B$_4$C EBSA (Figure 3a). It is known that the minimum surface roughness is crucial to ensure surface quality and increase the longevity of tools [27]. The methods of roughness reduction will be discussed later on.
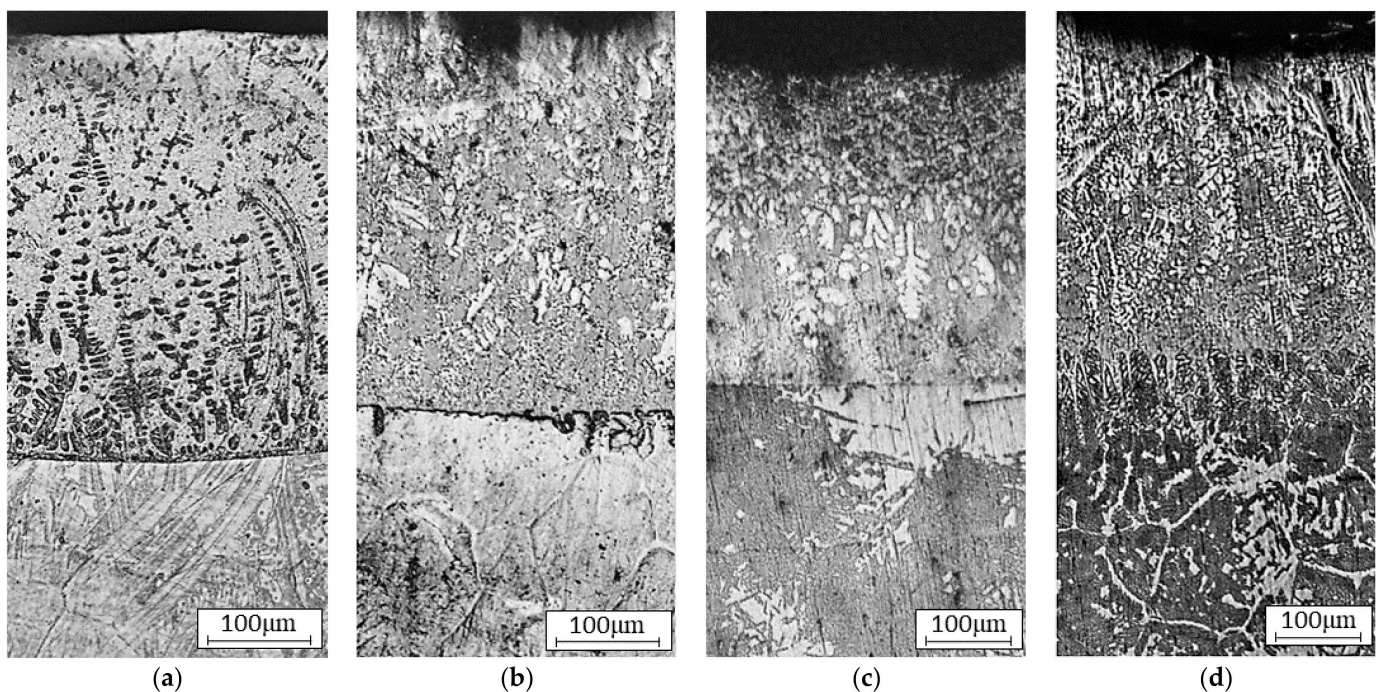

Figure 3. Microstructure of H21 and L6 steels after EBSA: (**a**) Sample No1; (**b**) Sample No2; (**c**) Sample No3; (**d**) Sample No4.

During the EB processing, the paste components and steel surfaces were heated to the melting point. The solidification process began immediately (the heating/cooling rate was about ~10^6 K/s) after switching off the EB, resulting in dendrite-like and eutectic structure

formation. Dendrites grew almost perpendicularly to the treated surface thermal fields. The layer on Sample No1 contained the longest dendrites stretching from the surface to the base metal and they were slightly less than the thickness of the whole layer (Figure 3a). Other dendrites on Samples No2–No4 were concentrated close to the surface and in the middle zones of the layers. One more distinctive feature was that only Sample No1 had dark dendrites while other samples contained white ones. This feature occurred due to phase composition difference, which will be further confirmed by the EDS analysis and microhardness test.

The interface between layers and the base metal had a distinct border except Sample No4. The developed transition zone was observed below the main layer on L6 steel after the two-component EBSA. It reached 80–100 μm thick as shown in Figure 3d. Moreover, Sample No4 contained sharp and long crystals on the surface. It is known that the EBSA of low-carbon steels by boron (electron beam boriding according to the authors' terminology) resulted in a layer with iron borides of elongated prismatic shape [3].

Microhardness tests of H21 steel showed that its hardness increased after the EBSA. The maximum microhardness of Sample No1 had been just over 900 HV; then, it gradually decreased to a low of around 650 HV in the base metal (Figure 4a). The minimum values on the graph at 50 and 150 μm from the surface corresponded to soft phases of the layers, which was a first axis of the dendrites. The similar microhardness distribution slope was obtained on Sample No2 with the minimum 50 μm from the surface (Figure 4b). However, the maximum microhardness was 1550 HV, which is 1.7 times higher than the maximum value on Sample No1.
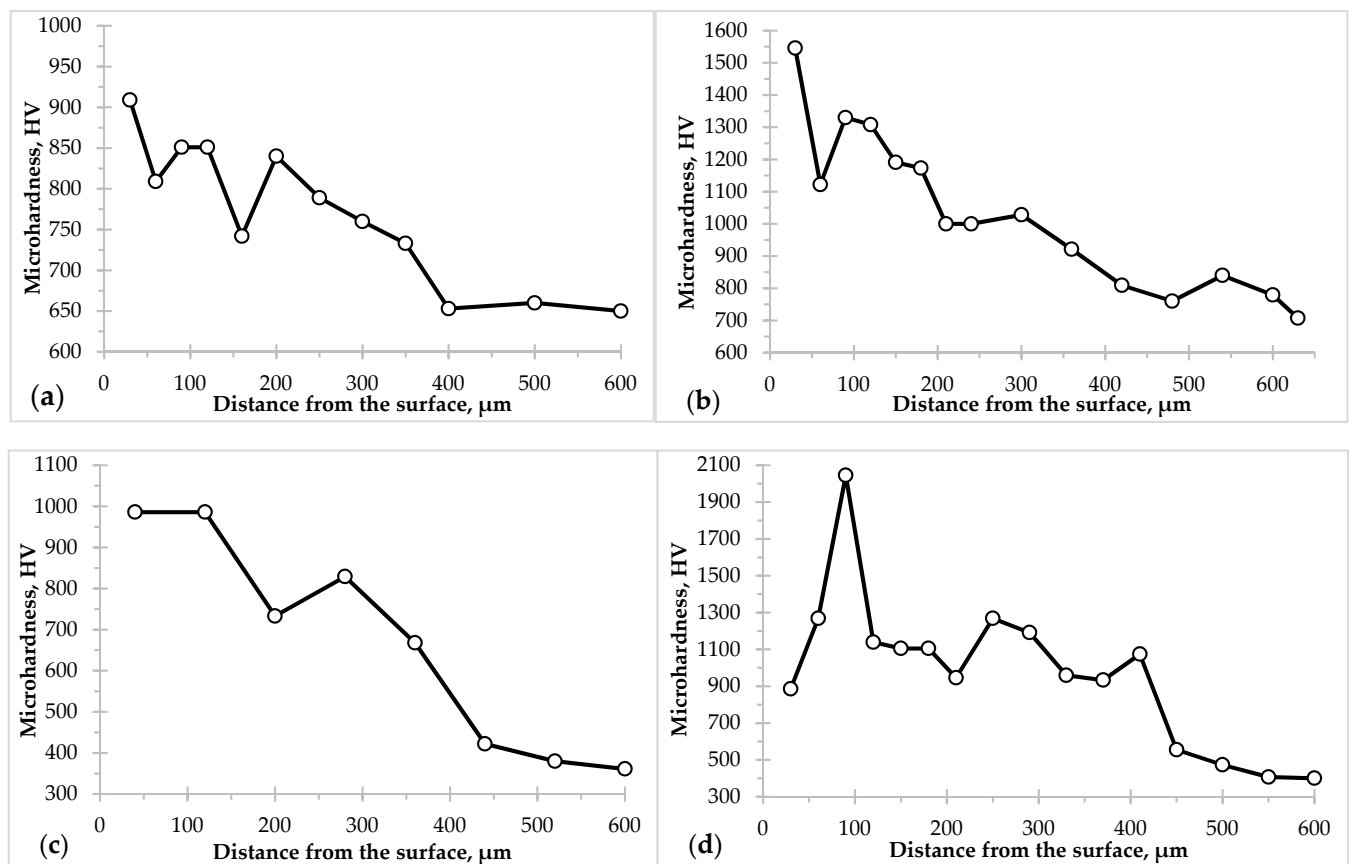

Figure 4. Microhardness distribution of H21 and L6 steels after the EBSA: (**a**) Sample No1; (**b**) Sample No2; (**c**) Sample No3; (**d**) Sample No4.

The microhardness of L6 steel after EBSA also increased. Its distribution slope on Sample No3 had a gentle curvature, starting from 1000 HV on the surface and gradually decreasing to 350 HV in the base metal (Figure 4c). The minimum value was at 200 μm from the surface, which corresponded to the area between solid dendrites.

The observed microhardness fluctuations in the layer on Sample No4 indicated a complex phase composition. On the surface, its value was about 900 HV; then, it rapidly increased to 2100 HV at a distance of 100 μm from the surface. Beyond that distance, microhardness varied in the range between 950 and 1250 HV in the layer and the transition zone before it went down to a low of 400 HV in the base metal.

The maximum microhardness of the layer on L6 steel exceeded the microhardness of H21 steel by 1.11 times after B_4C EBSA and 1.35 times after B_4C+Al EBSA. On the contrary, the microhardness of the base metal on H21 steel surpassed the microhardness of L6 steel approximately 1.7 times after the EBSA in both treatment pastes.

Mechanical properties of H21 steel are higher than on L6 steel. This advantage is due to H21 steel composition containing up to 15% of alloying elements (tungsten, chromium, etc.) mainly in the form of hard carbides. It is known that the hardness of H21 steel after quenching reaches 53 HRC, which is equal to 560 HV; as for L6 steel, it is 54–56 HRC, which is aligned with 580–615 HV [21,28,29]. Despite having relatively the same hardness, it is known that H21 steel's hardening response is higher than that of L6 steel [21]. Regarding our research, the base metal's microhardness was measured as 650–750 HV for H21 steel and 400–500 HV for L6 steel after the EBSA in both treatment pastes. Hence, the cooling rate was high enough for quenching of H21 steel and martensite transformation. Carbon displacement from the surface by paste components also contributed to higher H21 steel microhardness.

The microhardness difference on the steel surfaces referred to the phase composition of the layers. The XRD analysis showed iron borides presence in all samples and aluminum borides in Sample No4 (Figures 5–8). Iron carbide was revealed and contributed to its high microhardness. Chromium was revealed on H21 steel due to its higher content in the steel. Depending on the paste composition, aluminum-containing phases (AlFe, AlB_2) or boron carbides (B_4C, $B_{10}C$) were revealed in both steels after the EBSA in B_4C-Al or B_4C paste, respectively. Carbon was revealed as a result of boron carbide decomposition in a vacuum under electron beam irradiation (Figure 8).
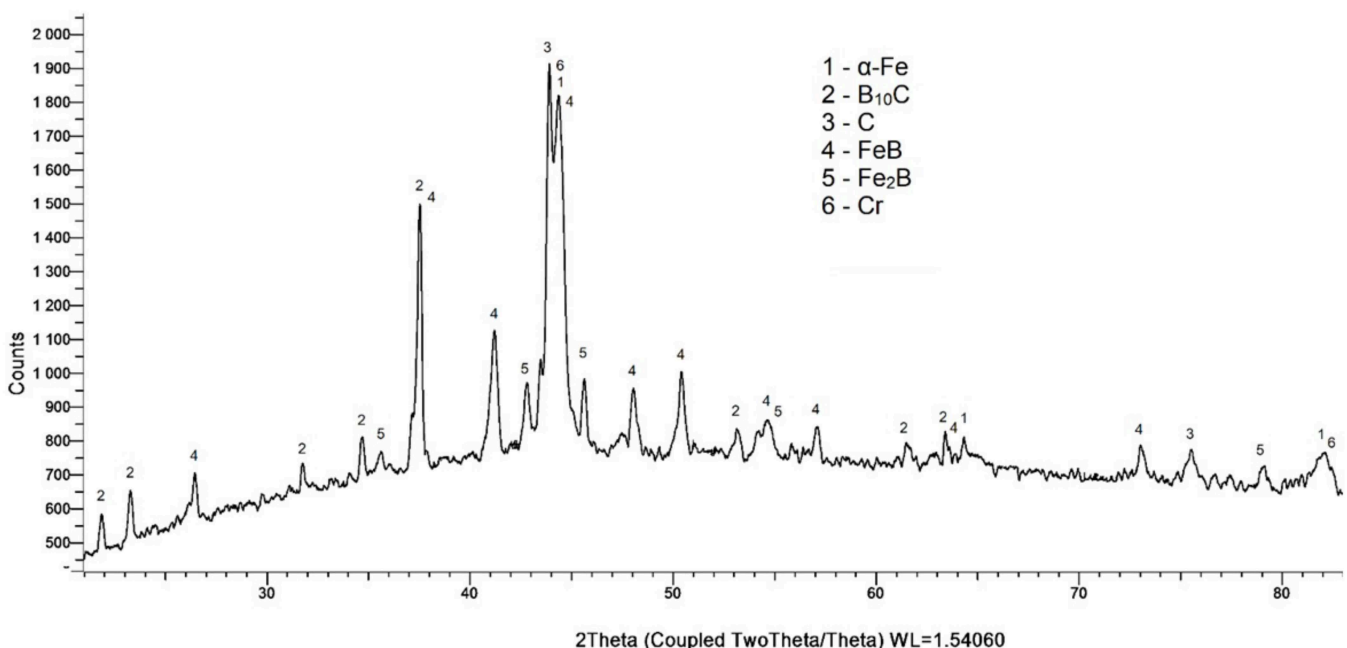

Figure 5. XRD pattern of H21 steel after B_4C EBSA.

As was mentioned above, the dendrites had different elemental compositions and microhardness. The EDS analysis of Sample No1 showed lower concentrations of W, Cr, and V inside the dendrites (spectrums 1–3) and higher content in the surrounding area (spectrums 4, 5) as shown in Table 5. For instance, tungsten concentration was approximately 4.5% and 13.8%, respectively. So, the layer consisted of solid α-Fe solutions in the form of dendrites surrounded by eutectic composition, where the latter was a mechanical mixture of α-Fe and carbides. The boron presence was confirmed only in local near-surface zones contradicting the XRD analysis results. Thus, iron borides formed local separate areas on the surface.
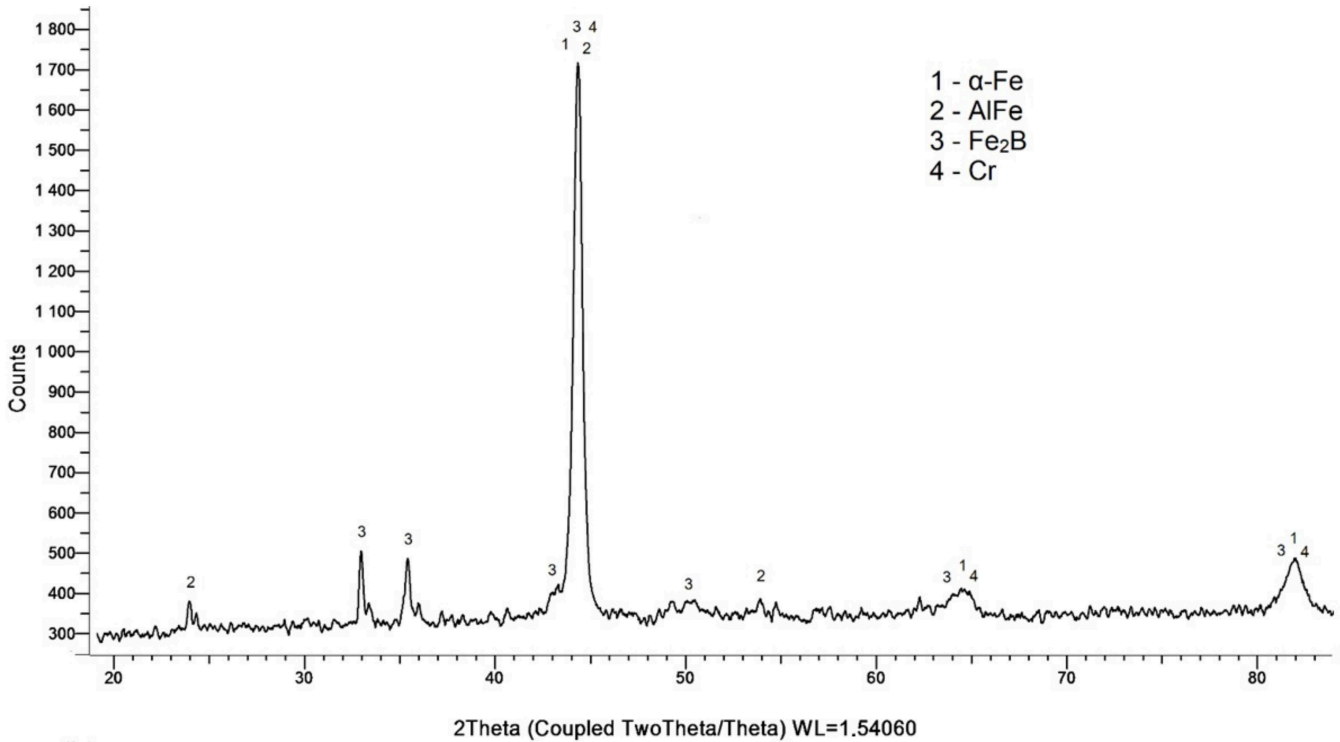

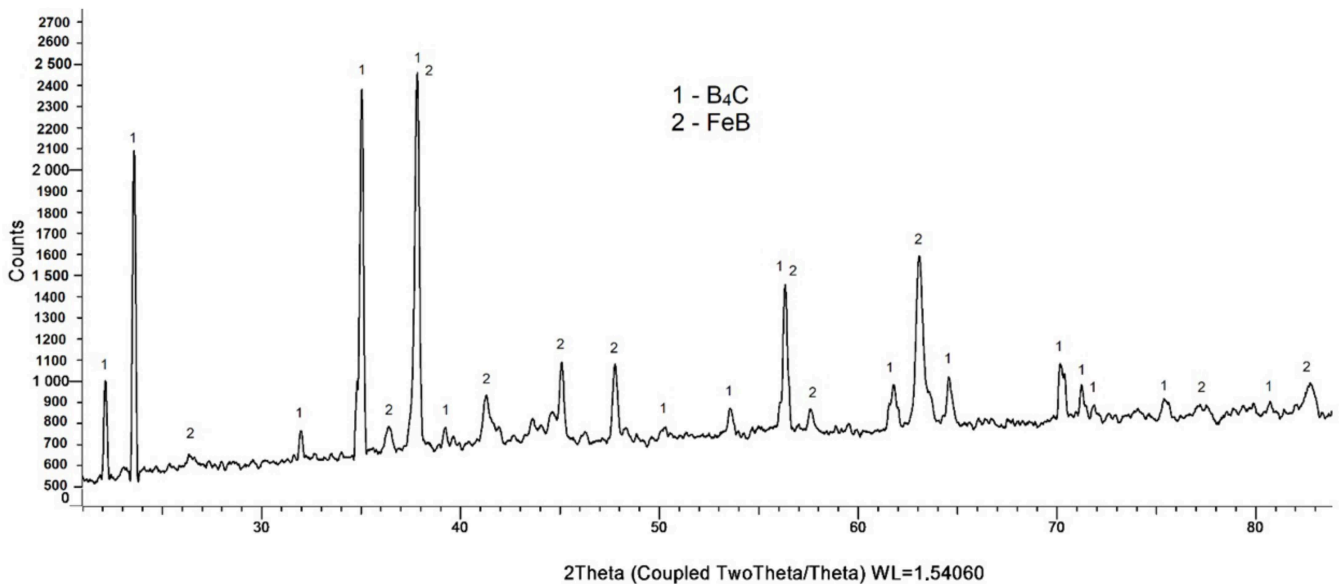**Figure 6.** XRD pattern of H21 steel after B_4C+Al EBSA.

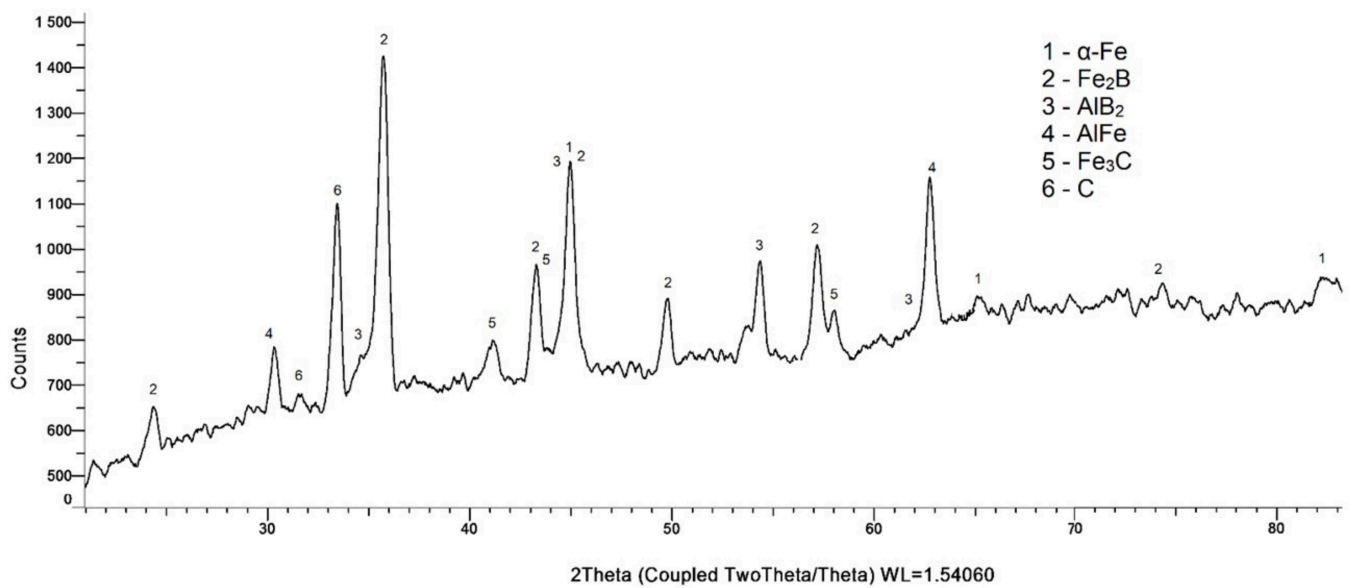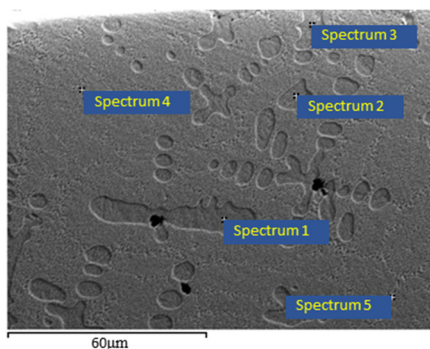**Figure 7.** XRD pattern of L6 steel after B_4C EBSA.

Figure 8. XRD pattern of L6 steel after B_4C+Al EBSA.

Table 5. The elemental composition of H21 steel after B_4C EBSA (Sample No1) in the near-surface zone.

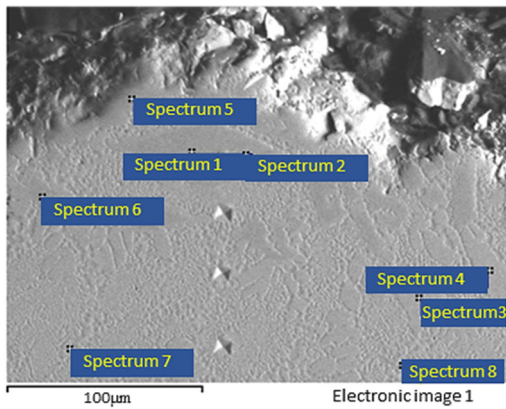| No Spectrum	Elemental Composition, wt %					Total
	C	V	Cr	Fe	W	
1	10.38	0.20	1.61	83.32	4.49	100
2	10.01	0.19	1.69	83.84	4.28	100
3	9.96	0.16	1.62	83.52	4.74	100
4	9.09	0.59	2.35	74.15	13.82	100
5	8.41	0.77	2.95	74.08	13.79	100
max	10.38	0.77	2.95	83.84	13.82	
min	8.41	0.16	1.61	74.08	4.28	

The SEM image of Sample No2 in near-surface zone showed cellular and rhombic crystals (electronic image in Table 6). It is known that iron borides form such structures during laser or electron beam irradiation of steel [30]. The EDS analysis (spectrums 1–4) showed that those crystals contained up to 5.65 % of B. The amount of B was less than its concentration in Fe_2B.

Other structural components were dendrites (spectrums 5, 6) and eutectic composition (spectrums 7, 8). Carbon and tungsten content was the lowest in rhombic crystals, average in dendrites, and highest in eutectic composition, while chromium content had opposite data (Table 6). Aluminum content was low and its maximum concentration was 0.26 % in the upper zone of the layer.

Two structural components were detected in the upper zone of the layer after B_4C EBSA: cellular crystals on top and eutectic composition below (electronic image in Table 7). The boron concentration reached 9.47% in cellular crystals and 3.42% in eutectic composition, while carbon content was about 3–8% and 11.12%, respectively. Boron content in the upper zones corresponded to Fe_2B [31]. Eutectic composition contained a mechanical mixture of carbides and solid α-Fe solution.

Table 6. The elemental composition of H21 steel after B$_4$C+Al EBSA (Sample No2) in near-surface zone.

No Spectrum	Elemental Composition, wt %							Total
	B	C	Al	V	Cr	Fe	W	
1	3.88	1.09	0.11	0.67	4.19	83.15	6.91	100
2	5.65	1.91	0.09	0.60	3.73	83.44	4.58	100
3	5.28	1.55	0.07	0.62	3.66	83.57	5.26	100
4	1.75	1.38	0.03	0.61	4.23	86.53	5.47	100
5	-	2.78	0.10	0.66	3.60	83.93	8.94	100
6	-	4.81	0.09	0.67	3.16	82.40	8.87	100
7	-	4.98	0.02	0.86	2.90	79.32	11.92	100
8	-	6.01	0.26	0.46	2.63	81.49	9.16	100
max	5.65	6.01	0.31	0.86	4.23	90.08	11.92	
min	0.10	0.87	0.02	0.34	1.96	79.32	4.58	

Table 7. The elemental composition of L6 steel after B$_4$C EBSA (Sample No3) in near-surface zone.

| No Spectrum	Elemental Composition, wt %							Total
	B	C	Si	Cr	Mn	Fe	Ni	
1	8.38	7.08	0.06	0.68	0.37	82.65	0.78	100
2	8.20	3.62	0.24	0.59	0.55	85.76	1.04	100
3	9.47	8.40	0.32	0.57	0.35	79.88	1.02	100
4	3.42	11.12	0.56	0.68	0.42	82.53	1.27	100
max	9.47	11.12	0.56	0.68	0.55	85.76	1.27	
min	3.42	3.62	0.06	0.57	0.35	79.88	0.78	
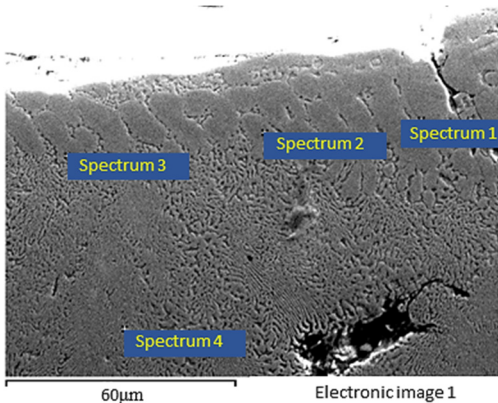
The EDS analysis of Sample No4 showed high boron and carbon concentration on the surface in spectrum 1, which confirmed boron carbide presence (Table 8). Spectrums 2 and 5 showed less boron content, which corresponded to the iron boride concentration. The maximum Al concentration was about 5% on the surface, which was related to solid solution of Al in α-Fe. The XRD analysis also showed AlFe. It is an ordered solid solution with Al concentration of 24–32.57 wt % and a simple cubic (B2-type) crystal structure [32,33]. Boron and Al concentration decreased gradually from the surface to the base metal on L6 steel as shown in Figure 9. There was no correlation between Al concentration and layer thickness on H21 steel, as it was stably low throughout the layer thickness. Boron content was twice lower on H21 steel than on L6 steel and had a similar slope.

Boron and aluminum content on L6 steel was higher than on H21 steel because of higher alloying concentration in the latter (up to 15.7% in H21 against up to 5.8% L6). The SEM images also revealed porosity due to boron carbide particles delamination during cross-section grinding and polishing. The XRD analysis detected that some pores contain carbon on Samples No1 and No4. Regarding boron distribution after B$_4$C EBSA, its content on L6 steel was higher than on H21 steel as well.

Table 8. The elemental composition of L6 steel after B_4C+Al EBSA (Sample No4) in near-surface zone.

No Spectrum	Elemental Composition, wt %									Total
	B	C	O	Al	Si	Cr	Mn	Fe	Ni	
1	62.58	35.98	1.21					0.24		100
2	11.14	9.07		5.13	0.94	0.50	0.54	70.65	2.01	100
3		63.54	23.21	0.06	0.09	0.24		12.86		100
4	3.59	8.30		0.71	0.29	0.65	0.54	84.60	1.32	100
5	10.50	9.23		1.10	0.46	0.47	0.46	76.16	1.62	100
6		7.16		0.43	0.04	0.73	0.54	90.14	0.94	100
7		9.02		0.67	0.35	0.56	0.53	87.63	1.24	100
8		10.05		1.01	0.32	0.55	0.54	86.10	1.42	
max	62.58	63.10	23.21	5.13	0.94	0.73	0.54	90.14	2.01	
min	62.58	7.16	1.21	0.06	0.04	0.24	0.46	0.24	0.94	
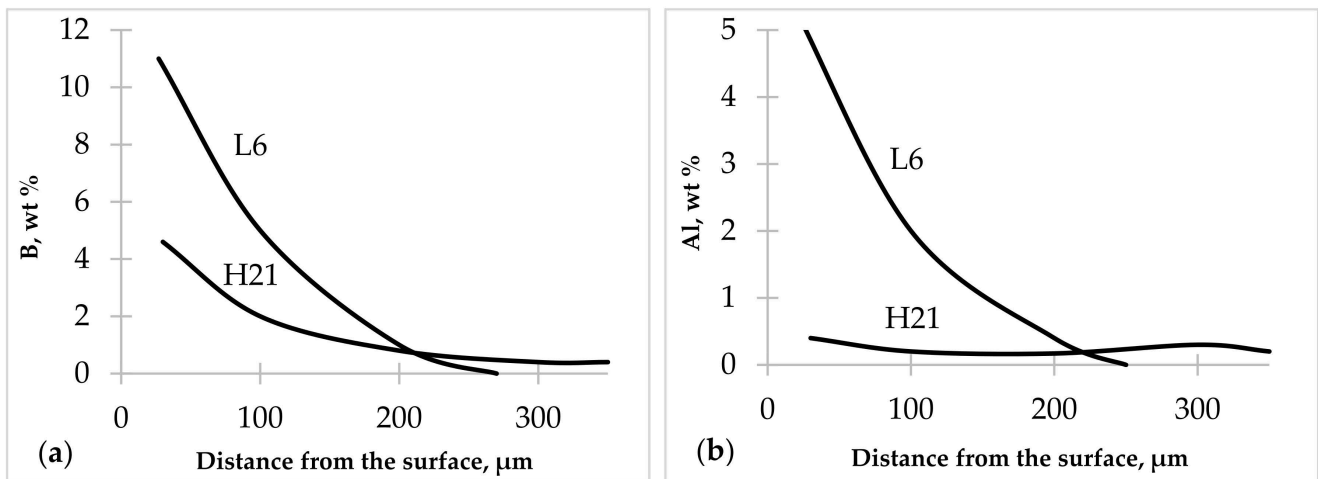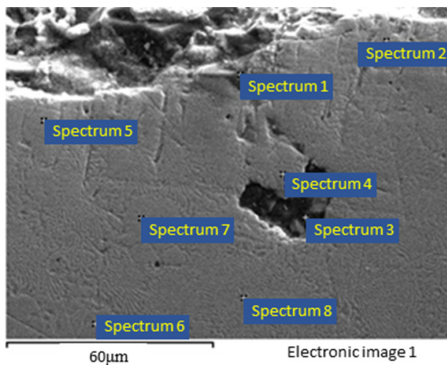
Figure 9. Boron (**a**) and aluminum (**b**) distribution in the layers of the tool steels after B_4C+Al EBSA.

3.1. Wear Resistance

The wear resistance test was carried on until dramatic mass loss was spotted, which indicated reaching the base metal and that the layer was no longer able to conduct its functional properties. On the graph, these critical points are characterized by steep rise of the curves.

The test results indicated that wear resistance of both steels after the EBSA significantly increased, as shown in Figure 10. Samples No1 and No4 demonstrated best results within 60 min of testing. After that time, Sample No4 showed better wear resistance behavior compared to Sample No1. Samples No2 and No3 showed moderate resistance to abrasive wear within 25 min and 40 min of testing, respectively. However, it should be noted that mass loss of Sample No2 was twice lower than that of Sample No3 within 25 min of testing. Consequently, the sharp mass loss occurred on Sample No2, while Sample No3 stayed more or less resistant to wear for another 15 min.
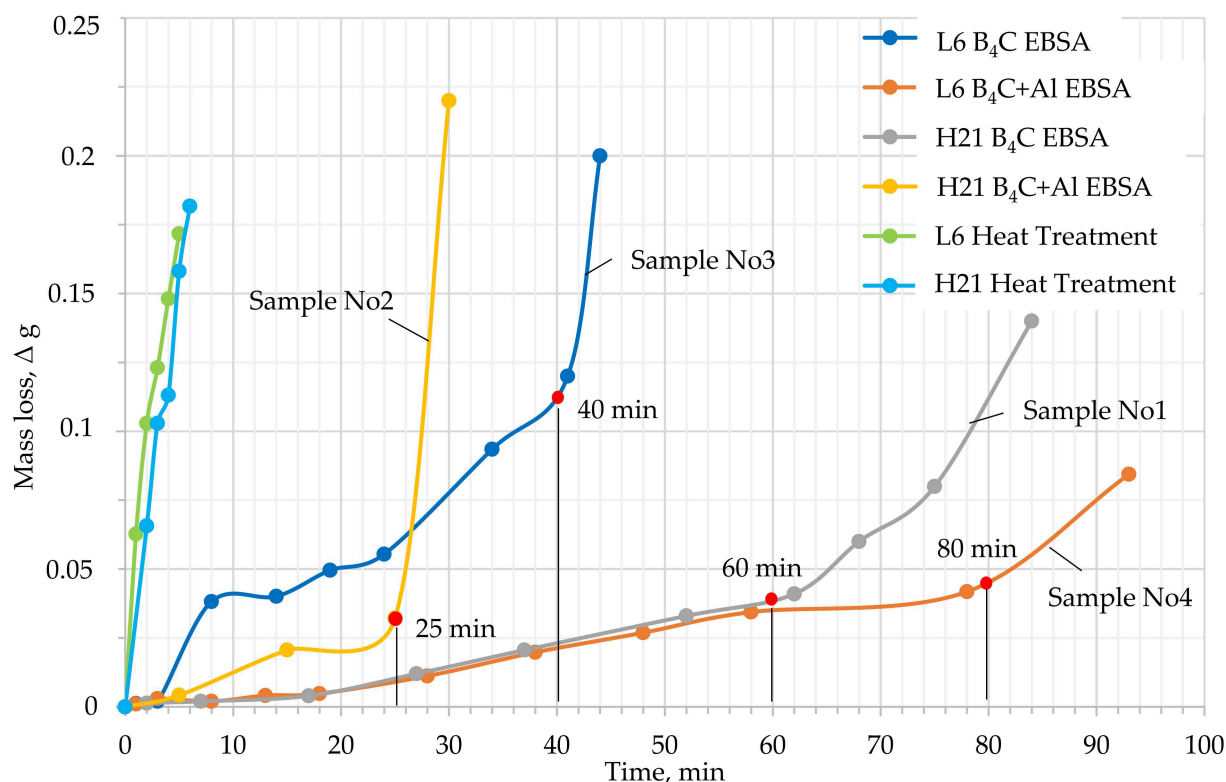
Figure 10. Wear resistance behavior of tool steels before and after the EBSA.

Steady wear resistance of H21 and L6 steels after the EBSA in B_4C and B_4C+Al pastes, respectively (Samples No1 and No4) was due to their diverse phase composition. Both samples contained an additional hard phase that neither of the samples contained. For instance, the XRD analysis revealed iron boride FeB in Sample No1 and aluminum boride AlB_2 in Sample No4 (Figures 5 and 8). Carbon was revealed in both samples as well. Its effect as a lubricant will be further discussed.

The EDS analysis showed that all samples' surfaces were severely oxidized (Tables 9–12). Friction-induced heating results in tribooxides formation [19,34]. Wear mechanism differs significantly depending on the alloying composition. After pure B_4C alloying, a high amount of boron and carbon was revealed on the surface of both steels as dark spots on SEM images (Figure 11). H21 steel was the least oxidized sample (up to 9.14% of O) and had a greater number of hard components on the surface compared to L6 steel (Table 9, Figure 11a). Denser alloying concentration in this type of steel also contributed to its strong wear and oxidation resistance (Figure 10). L6 steel contained more oxygen on the surface, up to 34 % of oxygen in spectrum 3 in bright iron oxide particle (Table 10, Figure 11b).

After finishing the wear test, Samples No2 and No4 were oxidized (Tables 11 and 12). Besides that, nitrogen was revealed on the worn surface of L6 steel. The SEM demonstrated that abrasion and delamination were major wear mechanisms for Samples No2 and No4 (Figure 12). Delamination craters on the worn surfaces were clearly seen in both steels. Spheroidized particles of 20–30 μm in diameter were visible on the surface of L6 steel in the delamination craters. These particles contained a high amount of carbon up to 51% and contributed to the high wear resistance of L6 steel as a lubricant. The delamination craters and high roughness created the condition for holding carbon particles. The self-lubrication process took place on the L6 steel after two-component alloying [35]. Wang et al. reported on a carbon barrier layer that turned into the TiC layer and retarded the interfacial reaction between active Ti and $Sc_2W_3O_{12}$-reinforced phases on stainless steel [36]. A similar mechanism can occur on the surface of tool steels where a carbon sublayer protects their surface against the counterpart as well as atmospheric oxygen and nitrogen.

Table 9. The elemental composition of worn surface on H21 steel after B$_4$C EBSA.

No Spectrum	Elemental Composition, wt %									Total
	B	**C**	**O**	**Si**	**V**	**Cr**	**Mn**	**Fe**	**W**	
1	17.23	11.38	9.14	2.05	0.27	1.62	-	54.40	3.89	100
2	42.73	18.95	9.03	5.39	0.16	0.74	0.19	20.67	2.13	100
3	-	4.22	6.75	-	0.46	2.23	-	79.21	7.12	100
max	42.73	18.95	9.14	5.39	0.46	2.23	0.19	79.21	7.12	
min	17.23	4.22	6.75	2.05	0.16	0.74	0.19	20.67	2.13	

Table 10. The elemental composition of worn surface on L6 steel after B$_4$C EBSA.

No Spectrum	Elemental Composition, wt %								Total
	B	**C**	**O**	**Si**	**Cr**	**Mn**	**Fe**	**Ni**	
1	35.42	26.23	22.62	0.18	-	-	11.65	3.89	100
2	36.00	27.44	25.39	0.15	-	-	8.48	2.55	100
3	-	6.19	34.07	0.27	-	0.51	58.96	-	100
4	-	5.45	4.92	-	0.51	0.49	87.11	1.52	100
5	-	5.87	7.55	-	0.50	0.46	83.79	1.82	100
max	36.00	27.44	34.07	0.27	0.51	0.51	87.11	3.89	
min	35.09	5.45	4.92	0.15	0.50	0.46	8.48	1.52	

Table 11. The elemental composition of worn surface on H21 steel after B$_4$C+Al EBSA.

No Spectrum	Elemental Composition, wt %							Total
	C	**O**	**Al**	**V**	**Cr**	**Fe**	**W**	
1	4.74	27.25	0.70	0.26	1.56	61.06	4.42	100
2	5.11	6.17	0.77	0.56	2.51	75.11	9.76	100
3	8.33	1.67	0.77	0.39	2.36	78.59	7.89	100
max	8.33	27.25	0.77	0.56	2.51	78.59	9.76	
min	4.74	1.67	0.70	0.26	1.56	61.06	4.42	

Table 12. The elemental composition of worn surface on L6 steel after B$_4$C+Al EBSA.

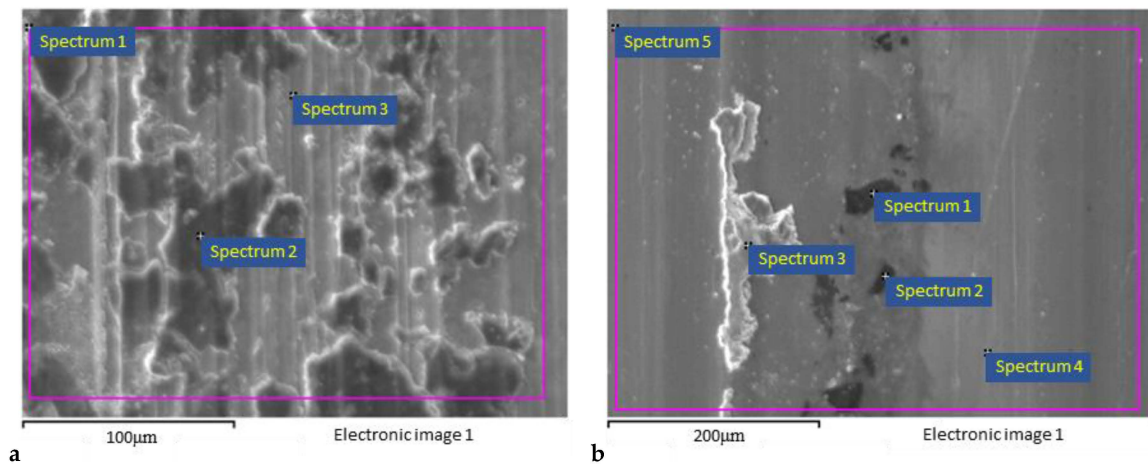| No Spectrum	Elemental Composition, wt %										Total
	C	**N**	**O**	**Al**	**Si**	**S**	**Cr**	**Mn**	**Fe**	**Ni**	
1	8.15	-	26.99	0.54	0.25	-	0.37	0.51	62.18	1.01	100
2	2.72	-	26.17	0.37	0.22	-	0.56	-	68.87	1.08	100
3	51.81	10.35	15.02	0.18	0.16	0.45	-	-	22.03	-	100
4	44.27	4.35	22.48	1.69	4.90	0.38	0.24	-	21.70	-	100
5	7.33	-	8.84	-	0.27	-	0.56	-	80.92	2.07	100
max	51.81	10.35	26.99	1.69	4.90	0.45	0.56	0.51	80.92	2.07	
min	2.72	4.35	8.84	0.18	0.16	0.38	0.24	0.51	21.70	1.01	

Figure 11. SEM images of worn surfaces on H21 (**a**) and L6 (**b**) steel after B$_4$C EBSA and wear test.
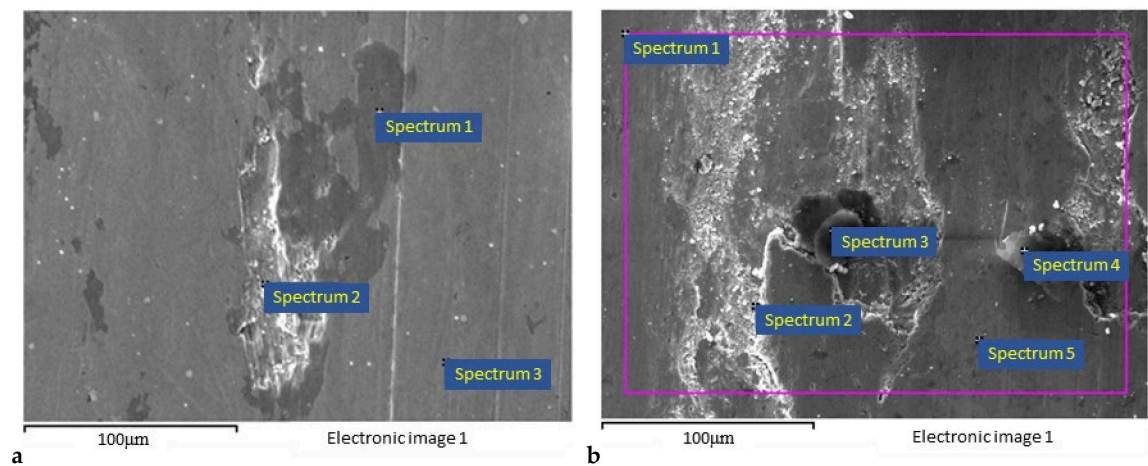

Figure 12. SEM images of worn surfaces on H21 (**a**) and L6 (**b**) steel after B$_4$C+Al EBSA and wear test.

3.2. Discussion

There was no difference in layer thickness depending on the steel type or paste composition after the EBSA. The layer thickness on L6 steel was three times higher than on H21 steel due to the higher concentration of alloying components in the latter steel [37]. It is known that alloying components retard diffusion of the penetrating elements (B, C, N, etc.) during different TCT methods [4]. Borides and carbides compete with each other during TCT processes due to low welding properties. Thus, carbon distribution is a systematic phenomenon for high-alloyed tool steels and it is driven by the insoluble nature of carbides in borides [38]. This is true not only for diffusion processes, but for the EBSA as well. Due to the lower concentration of the alloying elements in L6 steel, it has a higher concentration of hard phases compared to H21 steel. Boron and aluminum content was higher in L6 steel compared to H21 steel though the layer thickness was equal on both steels (Figure 9). The transition zone defined a liquid area during the EB heating. All samples had a clear border between the layer and the base metal except for L6 steel after B$_4$C+Al EBSA, where a transition zone was developed.

The treatment time of one-component EBSA was three times longer than that of B$_4$C+Al EBSA with the same layer thickness. It was established earlier that Al promoted diffusion processes during common boroaluminizing in furnace [19]. Two-component EBSA results in more complex microstructure and phase diversity of the layers on L6 steel. This phenomenon needs to be further investigated. It should be noted that the microhardness of the layer and the base metal after two-component alloying (B$_4$C + Al)

was higher than after alloying with only B_4C. Obviously, this was due to aluminum in the surface layer leading to solid aluminum phases such as AlB_2 [39]. Other factors promoting microhardness of both steels are structural transformations (quenching) from the liquid state, thermal stresses contributing to phase hardening, and plastic deformation. Carbon displacement from the surface by B and Al contributed to higher H21 steel microhardness in base metal compared to L6 steel [40].

Surface properties modification by EB heating with saturating mixtures leads to more plastic layers in comparison with the layers obtained by conventional TCT [41]. The surface of the steels after EB treatment has a heterogeneous structure that combines hard (brittle) and more ductile structural components. This combination partially explains the absence of thermal cracks when the steel surface is subjected to high temperatures, approximately 2000 K. Heating to this temperature inevitably brings the melting of the steel's surface under study, together with the applied paste. As a result of subsequent crystallization, a dendritic structure is formed (mainly in the upper parts of the layers). The morphology and structure of the layers after single-component EBSA are explained using the Fe–B phase diagram, where each zone of the layer is considered to have a certain composition [15]. In the case of two-component EBSA, this approach can be used partially or can be completely excluded due to the high content of alloying components. There is a need to study triple Fe–B–Al or four-component Fe–B–Al–C phase diagrams.

SEM images in Tables 4–7 showed that all samples have porosity in the depth of 50–60 μm from the surface, induced by B_4C particles delamination during the sample preparation procedure. Other black spots on SEM images are carbon particles. These particles contributed the most to wear resistance improvement of H21 and L6 steels after the EBSA in B_4C and B_4C+Al pastes, respectively. A rough worn-out surface promotes carbon particles retention and results in the self-lubrication process on L6 steel after two-component alloying. It is known that the grooves on the inner surface of the journal bearing accomplish the function in the same way [42,43]. Such surface texture amplifies hydrodynamic lubrication and enhances the tribological contact performance for a wide range of applications [44].

Regarding high roughness on the surface of the layers, jig grinding by the cubic boron nitride (CBN) cutting tool on a vertical milling machine improved surface quality of tool steels after the EBSA processes. Applying CBN grinding as a final mechanical operation resulted in roughness reduction from initial Ra 4 μm for boriding and Ra 7.7 μm for boroaluminizing to Ra 0.09 μm and Ra 0.43 μm, respectively [27]. The provided surface quality ensures the operational properties of hot-work tool steels. It determines further industrial application of the conducted research in metal forming processes such as stamping. It is planned to modify the working surfaces of the U-bending die, as shown in Figure 1, to prevent its intense degradation during the repeated billet deformation.

The self-lubricating process, recognized on the surface of L6 steel after the EBSA in B_4C+Al, needs further verification. Coefficient of friction (COF) measurement will confirm the process and reflect its behavior over time. A ball-on-disk tribometer will be used for carrying out evaluation of the COF against time [45]. The counter face sliding partner will be the AISI E52100 high-carbon chromium alloy ball of 6 mm diameter, which is expected to perform well against wear-resistant boron-containing layers.

4. Conclusions

The EBSA significantly improved wear resistance and hardness of H21 and L6 tool steels. The most wear-resistant layer was obtained on L6 steel after the EBSA in B_4C+Al paste due to its high microhardness (up to 2100 HV) and carbon particles on the surface.

Al added to B_4C paste shortens the duration of the EBSA process and improves the mechanical properties of both steels compared to the EBSA in single B_4C paste.

References

1. Valkov, S.; Ormanova, M.; Petrov, P. Electron-Beam Surface Treatment of Metals and Alloys: Techniques and Trends. *Metals* **2020**, *10*, 1219. [CrossRef]
2. Krukovich, M.G.; Prusakov, B.A.; Sizov, I.G. Plasticity as the Key to the Durability of Boronized Layers. In *Plasticity of Boronized Layers*; Springer Series in Materials Science; Springer: Cham, Switerland, 2016; Volume 237, pp. 65–80. [CrossRef]
3. Krukovich, M.G.; Prusakov, B.A.; Sizov, I.G. The Structure Compositeness as the Foundation for the Plasticity of Boronized Layers. In *Plasticity of Boronized Layers*; Springer Series in Materials Science; Springer: Cham, Switerland, 2016; Volume 237, pp. 197–227. [CrossRef]
4. Dearnley, P. Surface Engineering with Diffusion Technologies. In *Introduction to Surface Engineering*; Cambridge University Press: Cambridge, UK, 2017; pp. 35–115. [CrossRef]
5. Ostapenko, M.G.; Semin, V.O.; D'yachenko, F.A.; Neiman, A.A.; Meisner, L.L. Structure and residual stress distribution in TiNi substrate after fabrication of surface alloy using electron-beam treatments. *Acta Mater.* **2022**, *231*, 117893. [CrossRef]
6. Altan, T. Selection of die materials and surface treatments for increasing die life in hot and warm forging. In Proceedings of the Tech Conference, Paper No 644-FIA, April 2011. Available online: https://www.forging.org/uploaded/content/media/Altan_paper_Die_materials_and_surface_treatments6.pdf (accessed on 30 March 2022).
7. Fuchs, K.D. Hot-work tool steels with improved properties for die casting applications. In Proceedings of the 6th International Tooling Conference, Washington, DC, USA, 27–29 April 2009; p. 183.
8. Kulka, M.; Mikołajczak, D.; Dziarski, P.; Panfil-Pryka, D. Laser Surface Alloying of Austenitic 316L Steel with Boron and Some Metallic Elements: Properties. *Materials* **2021**, *14*, 2987. [CrossRef] [PubMed]
9. Gromov, V.E.; Ivanov, Y.F.; Glezer, A.M.; Kormyshev, V.E.; Konovalov, S.V. Electron-beam modification of a surface layer deposited on low-carbon steel by means of arc spraying. *Bull. Russ. Acad. Sci. Phys.* **2017**, *81*, 1353–1359. [CrossRef]
10. Nakajo, H.; Nishimoto, A. Boronizing of CoCrFeMnNi High-Entropy Alloys Using Spark Plasma Sintering. *J. Manuf. Mater. Process.* **2022**, *6*, 29. [CrossRef]
11. Kartal, G.; Timur, S.; Sista, V.; Eryilmaz, O.L.; Erdemir, A. The Growth of Single Fe_2B Phase on Low Carbon Steel via Phase Homogenization in Electrochemical Boriding (PHEB). *Surf. Coat. Technol.* **2011**, *206*, 2005–2011. [CrossRef]
12. Mishigdorzhiyn, U.L.; Sizov, I.G.; Polaynsky, I.P. Formation of coatings based on boron and aluminum on the surface of carbon steels by electron beam alloying. *Obrab. Met.-Met. Work. Mater. Sci.* **2018**, *20*, 87–99. [CrossRef]
13. Mertgenç, E.; Kayalı, Y.; Talaş, Ş. Effect of Boronizing and Aluminizing on the Wear Resistance of Steel AISI 1010. *Met. Sci. Heat Treat.* **2021**, *63*, 388–395. [CrossRef]
14. Chesnokov, A.E.; Smirnov, A.V.; Klinkov, S.V.; Kosarev, V.F. Preparation of the Composite Powder Al–B_4C by Ball Milling for Cold Spray. *J. Phys. Conf. Ser.* **2021**, *1945*, 012033. [CrossRef]
15. Zenker, R.; Buchwalder, A. *Elektronenstrahl-Randschichtbehandlung: Innovative Technologien für höchste industrielle Ansprüche*; Pro-beam: Freiberg, Germany, 2010; pp. 49–54.
16. Zenker, R. Electron Beam Surface Technologies. In *Encyclopedia of Tribology*; Wang, Q.J., Chung, Y.W., Eds.; Springer: Boston, MA, USA, 2013. [CrossRef]
17. Zenker, R.; Buchwalder, A. Electron beam surface hardening. In *ASM Handbook, Steel Heat Treating Fundamentals and Processes*; Dossett, J.L., Totten, G.E., Eds.; ASM International: Novelty, OH, USA, 2013; Volume 4A, pp. 462–475. [CrossRef]
18. Buchwalder, A.; Zenker, R. Pre- and post-surface treatments using electron beam technology for load-related application of thermochemical and PVD hard coatings on soft substrate materials. *Surf. Coat. Technol.* **2019**, *375*, 920–932. [CrossRef]
19. Mishigdorzhiyn, U.; Chen, Y.; Ulakhanov, N.; Liang, H. Microstructure and Wear Behavior of Tungsten Hot-Work Steel after Boriding and Boroaluminizing. *Lubricants* **2020**, *8*, 26. [CrossRef]
20. Mishigdorzhiyn, U.; Sizov, I. The Influence of Boroaluminizing Temperature on Microstructure and Wear Resistance in Low-Carbon Steels. *Mater. Perform. Charact.* **2018**, *7*, 252–265. [CrossRef]

21. Roberts, G.A.; Kraus, G.; Kennedy, R.L. *Tool Steels, Materials Park*; ASM International: Novelty, OH, USA, 1998.
22. Højerslev, C. *Tool Steels*; Forskningscenter Risoe. Risoe-R, No. 1244 (EN); Risø National Laboratory: Roskilde, Denmark, 2001. Available online: http://orbit.dtu.dk/files/7728903/ris_r_1244.pdf (accessed on 30 March 2022).
23. Lisovsky, A.L.; Pletnev, I.V. Razrabotka tekhnologii lazernogo uprochneniya shtampovoy osnastki [Development of technology for laser hardening of die equipment]. *Bull. Polotsk State Univ. Ser. B Appl. Sci.* **2008**, *2*, 65–72.
24. Grigoriev, Y.V.; Semenov, A.P.; Narhinov, V.P. Moshchnaya plavil'naya tekhnologicheskaya pech's elektronno-luchevym nagrevom [Powerful melting technological furnace with electron beam heating]. In *Integrated Use of Mineral Raw Materials of Transbaikalia*; Publishing House of the BSC SB RAS: Ulan-Ude, Russia, 1992; pp. 139–148.
25. Ivanov, Y.F.; Teresov, A.D.; Petrikova, E.A.; Ivanova, O.V.; Romanov, D.A. Razrabotka kompleksnoy metodiki borirovaniya nerzhaveyushchey stali kontsentrirovannymi potokami energii [Development of a complex technique for boriding stainless steel with concentrated energy flows]. In Proceedings of the 13th International Conference on Interaction of Radiation with a Solid Body, Minsk, Belarus, 21–24 September 2019; pp. 251–254.
26. Sizov, I.G.; Mishigdorzhiyn, U.L.; Maharov, D.M. A Study of Thermocycling Boroaluminizing of Carbon Steels. *Met. Sci. Heat Treat.* **2012**, *53*, 592–597. [CrossRef]
27. Ulakhanov, N.S.; Mishigdorzhiyn, U.L.; Greshilov, A.D.; Tikhonov, A.G.; Ryzhikov, I.N. Surface Processing Technology in Improving Operational Properties of Hot-Work Tool Steel. *Adv. Eng. Res.* **2019**, *188*, 362–366. [CrossRef]
28. Mesquita, R.A. *Tool Steels: Properties and Performance*, 1st ed.; CRC Press: Boca Raton, FL, USA, 2016. [CrossRef]
29. Nurbanasari, M.; Tsakiropoulos, P.; Palmiere, E.J. Influence of high temperature deformation and double tempering on the microstructure of a H21 tool steel. *Mater. Sci. Eng.* **2013**, *570*, 92–101. [CrossRef]
30. Bartkowska, A.; Bartkowski, D.; Swadźba, R.; Przestacki, D.; Miklaszewski, A. Microstructure, chemical composition, wear, and corrosion resistance of $FeB–Fe_2B–Fe_3B$ surface layers produced on Vanadis-6 steel using CO_2 laser. *Int. J. Adv. Manuf. Technol.* **2018**, *95*, 1763–1776. [CrossRef]
31. von Goldbeck, O.K. Iron—Boron Fe—B. In *IRON—Binary Phase Diagrams*; Springer: Berlin/Heidelberg, Germany, 1982. [CrossRef]
32. Li, X.; Scherf, A.; Heilmaier, M.; Stein, F. The Al-Rich Part of the Fe-Al Phase Diagram. *J. Phase Equilib. Diffus.* **2016**, *37*, 162–173. [CrossRef]
33. Lyakishev, N.P. *Phasovie Diagrammi Binarnikh Metallicheskikh System [Phase Diagrams of Binary Metallic Systems]*; Mashinostroenie: Moscow, Russia, 1996; p. 992.
34. Kisuka, F.; Wu, C.-Y.; Hare, C. Friction-induced heat generation between two particles. *EPJ Web Conf.* **2021**, *249*, 05007. [CrossRef]
35. Shah, F.U.; Glavatskih, S.; Antzutkin, O.N. Boron in Tribology: From Borates to Ionic Liquids. *Tribol. Lett.* **2013**, *51*, 281–301. [CrossRef]
36. Wang, P.; Xu, Z.; Liu, X.; Wang, H.; Qin, B.; Lin, J.; Cao, J.; Qi, J.; Feng, J. Regulating the interfacial reaction of $Sc_2W_3O_{12}/AgCuTi$ composite filler by introducing a carbon barrier layer. *Carbon* **2022**, *191*, 290–300. [CrossRef]
37. Ulakhanov, N.S.; Mishigdorzhiin, U.L.; Tikhonov, A.G.; Shustov, A.I.; Pyatykh, A.S. Modifikatsiya poverkhnostnogo sloya shtampovykh staley sozdaniyem B-Al–sloyev khimiko-termicheskoy obrabotkoy [Modification of the surface layer of die steels by creating B-Al-layers by chemical-thermal treatment]. *Hardening Technol. Coat.* **2021**, *12*, 557–564. [CrossRef]
38. Jurči, P.; Hudáková, M. Diffusion Boronizing of H11 Hot Work Tool Steel. *J. Mater. Eng. Perform.* **2011**, *20*, 1180–1187. [CrossRef]
39. Ramos, G.; Manzano, R.; Suárez, O.M. A comparative hardness study of $Al-Si/AlB_2$ and $Al-Si/AlB_{12}$ composites. *Sci. Eng. Compos. Mater.* **2012**, *19*, 67–73. [CrossRef]
40. Chander, S.; Chawla, V. Characterization and Industrial Performance Evaluation of Duplex-Treated AISI H21 Die Steel during Hot Forging Process. *Mater. Perform. Charact.* **2019**, *8*, 197–210. [CrossRef]
41. Sizov, I.G.; Smirnyagina, N.N.; Semenov, A.P. Special features of electron-beam boronizing of steels. *Met. Sci. Heat Treat.* **1999**, *41*, 516–519. [CrossRef]
42. Xie, Z.; Wang, X.; Zhu, W. Theoretical and experimental exploration into the fluid structure coupling dynamic behaviors towards water-lubricated bearing with axial asymmetric grooves. *Mech. Syst. Signal Process.* **2022**, *168*, 108624. [CrossRef]
43. Lin, Q.; Wei, Z.; Wang, N.; Chen, W. Analysis on the Lubrication Performances of Journal Bearing System Using Computational Fluid Dynamics and Fluid–Structure Interaction Considering Thermal Influence and Cavitation. *Tribol. Int.* **2013**, *64*, 8–15. [CrossRef]
44. Gropper, D.; Wang, L.; Harvey, T.J. Hydrodynamic lubrication of textured surfaces: A review of modeling techniques and key findings. *Tribol. Int.* **2016**, *94*, 509–529. [CrossRef]
45. Asthana, P.; Liang, H.; Usta, M.; Ucisik, A.H. Wear and Surface Characterization of Boronized Pure Iron. *J. Tribol.* **2007**, *129*, 1–10. [CrossRef]